On the Near-Field Spherical Wave Formation in Resonant Leaky-Wave Antennas Application to Small Lens Design

Bosma, Sjoerd; Neto, Andrea; Llombart, Nuria

DOI
10.1109/TAP.2021.3137238

Publication date
2022

Document Version
Final published version

Published in
IEEE Transactions on Antennas and Propagation

On the Near-Field Spherical Wave Formation in Resonant Leaky-Wave Antennas: Application to Small Lens Design

Sjoerd Bosma, *Graduate Student Member, IEEE*, Andrea Neto, *Fellow, IEEE*, and Nuria Llombart, *Fellow, IEEE*

***Abstract*— In this work, we show that the near field of leaky-wave resonant antennas (LWAs) radiating into a dense medium can be locally represented as a spherical wave in a certain solid angle around broadside using an accurate definition of the phase center. The near field in this solid angle can be efficiently evaluated through the integration of the spectral Green's function along the steepest descent path (SDP). Beyond this solid angle, defined as the shadow boundary angle, a residual contribution due to the leaky-wave pole must also be added to fully describe the near field. It is found that this shadow boundary angle can be used to define the phase center and geometry of a truncated lens that couples well to leaky-wave antennas, even in electrically small-to-medium sized lenses and low-contrast cases. To demonstrate the applicability of the proposed study, we combine the SDP field calculation with a Fourier optics (FO) methodology to evaluate the aperture efficiency and radiation patterns of small-to-medium sized lenses in reception. A truncated silicon lens with a diameter of only four free-space wavelengths is presented with almost 80% aperture efficiency. Excellent agreement with full-wave simulations is achieved, which demonstrates the accuracy of the proposed design and analysis methodology.**

***Index Terms*— Leaky-wave antennas, lens antennas, near fields, phase center, spherical wave.**

I. Introduction

LEAKY-WAVE resonant antennas (LWAs), also called Fabry Pérot antennas, have been widely studied in the literature to increase the directivity from a small source by using a planar stratification consisting of a dielectric [1] or metallic [2] superstrate. Multiple demonstrations of these antennas have been shown at various frequencies up to the submillimeter wave spectral region [3]–[7]. A fundamental trade-off between the directivity and bandwidth of these antennas exists, which depends on the level of reflection between the cavity and superstrate [8], [9]. In the literature, shielded cavities [10] and the addition of lenses [11], [12] or phase-correcting geometries [13], [14] have been proposed to increase the directivity of these classic geometries without compromising the bandwidth.

At mm- and sub-mm wave frequencies, when scanning to limited angles is required, there is an interest of developing sparse arrays to reduce the integration complexity [15]–[18]. Leaky-wave antennas with overlapped feeds have been proposed for improving the performances of sparse arrays [8], [19]–[21] where sparse arrays with periodicities in the order of a free-space wavelength (λ_0), bandwidths smaller than 10%, and scanning angles of at most 10° have been demonstrated. Larger periodicities will only come at the cost of even smaller bandwidths in such geometries. For example, sparse leaky-wave phased arrays with a period of $2\lambda_0$ will have less than 5% bandwidth as shown in [21]. In [16] and [17], the use of leaky wave antennas with dielectric lenses was proposed to enable sparse arrays with large periodicity ($>2\lambda_0$), wide bandwidth (35%), and larger scanning angles up to $\pm 25°$. One of the difficulties that arises in the design of such small size lenses or phase-correcting structures in combination with resonant leaky-wave feeds is the efficient evaluation of the leaky-wave near-field [17].

Most of the works in the literature on leaky-wave or Fabry–Pérot antennas consider only the far-field radiation patterns of the feed [1], [8], [9], [11], [22] and often make approximations on the solutions of the potentials in stratified media [1], [22]. For lenses that are small to medium in diameter (i.e., smaller than $\approx 15\lambda_0$, where λ_0 is the free-space wavelength) fed by leaky-wave feeds, as in the lens-phased array application [16], [17], the lens surface is in the near field of the feed. The design of such lenses has previously been approached as a parametric optimization by combining Physical Optics with full-wave simulations [23] or full-wave simulations with optimization algorithms [12] for other phase-correcting geometries.

In this article, we describe a way to design such lenses without the need for time-consuming full-wave simulations. To achieve this, we derive the shape of the lenses directly from the propagation constants of the leaky-wave modes. For that purpose, we use a spectral-domain method to efficiently and accurately compute the near-field radiation patterns, which, additionally, brings the needed physical insight. The spectral

Manuscript received February 10, 2021; revised June 15, 2021; accepted July 2, 2021. Date of publication December 28, 2021; date of current version February 3, 2022. This work was supported by the European Research Council (ERC) Starting Grant LAA-THz-CC (639749). *(Corresponding author: Sjoerd Bosma.)*

The authors are with the Department of Microelectronics, Faculty of Electrical Engineering, Mathematics and Computer Science (EEMCS), Delft University of Technology, 2628 CD Delft, The Netherlands (e-mail: s.bosma@tudelft.nl).

Color versions of one or more figures in this article are available at https://doi.org/10.1109/TAP.2021.3137238.

Digital Object Identifier 10.1109/TAP.2021.3137238

analysis decomposes the near field of these antennas into the summation of a branch contribution or space wave that can be evaluated by an integration over the steepest descent path (SDP) when a proper phase center is introduced, and multiple leaky-wave modal fields, associated with poles that are captured in the deformation into the SDP [24, p. 468].

The asymptotic decomposition of the near field in leaky-wave antennas was previously investigated in a different configuration, based on a single-mode leaky-wave slot antenna [25], where the phase center is stable and coincident with the feeding point of the antenna. It has also been applied to a very high contrast resonant leaky-wave antenna in [26] (equivalent to an air cavity with an infinite medium of $\varepsilon_r = 100$) as well as to other resonant leaky-wave antennas [27]–[29]. For a resonant LWA, the phase center is not coincident with the feeding point [30]. Moreover, in these later works no explicit link has been made between the space-wave near-field evaluation and the phase center of the LWAs. Here, we will extend this analysis to the understanding of the formation of a clean spherical wave in the near field by making this link, also for low contrast cases, where the leaky wave poles lie far away from the real axis.

We show that the near field in resonant LW antennas is well modeled by a spherical wave in a solid angle Ω_{SB} around broadside emanating from the phase center located far below the ground plane. We find that, also for points close to the source, the space–wave contribution to the total field can be calculated by integration over the SDP when the reference system is chosen to coincide with the phase center of the antenna, located at Δz. Both the solid angle, Ω_{SB}, of the spherical-wave representation and the phase center can be defined with the knowledge of the shadow boundary angle defined by the SDP deformation angle.

The spectral analysis gives a physical insight into the formation of the local spherical wave and leads to the derivation of an analytical geometry of an ideal lens, with high aperture efficiency, which is defined using only the propagation constants of the main leaky-wave poles. Moreover, the SDP integration can then be efficiently combined with a Fourier optics (FO) approach to calculate the aperture efficiency and radiation patterns of the lens-coupled leaky-wave antenna in reception [11], [31]. The combined method is computationally very fast and shows excellent agreement with full-wave lens simulations, removing the need for time-consuming parametric analyses as in [12] and [23].

The rest of this article is structured as follows. Section II describes the geometry under consideration and introduces the near-field spectral approach. In Section III, the near field is decomposed into the sum of an SDP contribution and (multiple) LW contributions. In Section IV, the phase center of resonant LWAs is discussed, which brings physical insight into the decomposition of Section III. In Section V, we show that the near field can be considered a local spherical wave in the solid angle Ω_{SB} around broadside. The near-field spherical wave representation is combined with an FO approach in reception in Section VI to evaluate the lens efficiency and radiation patterns of electrically small lenses. Conclusions are drawn in Section VII.

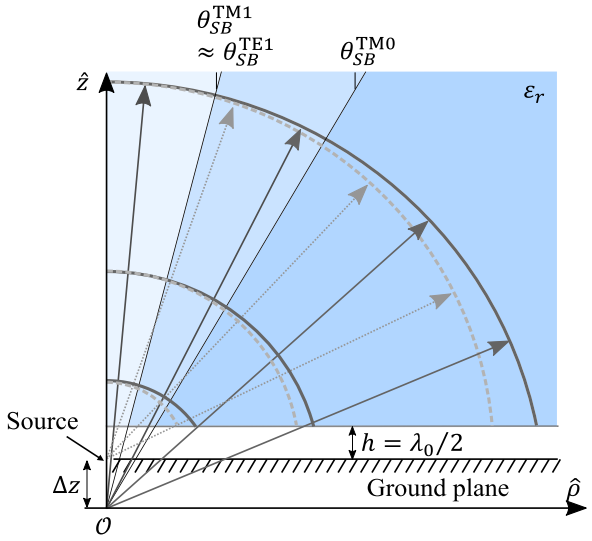

Fig. 1. Cross section of the geometry considered in this contribution with a semi-infinite dielectric separated from a ground plane (containing the source) by a $h = \lambda_0/2$ air cavity. The origin of the reference system is Δz below the source. The shaded blue regions are separated by the shadow boundary associated with the leaky-wave modes. The solid and dashed semicircles and associated arrows are centered at O and the source, respectively.

II. Problem Statement

The physical phenomenon exploited in a standard resonant LWA is the excitation of a pair of nearly degenerate TM_1/TE_1 leaky-wave modes inside a resonant dielectric cavity [1], such as air, placed between a ground plane and a partially reflecting surface. These modes propagate radially by means of multiple reflections along the cavity, leaking at the same time energy into the infinite air medium. This effect increases the antenna's effective area and thus its directivity. In [7], it was shown that an enhancement in the $bandwidth \times directivity$ performance of a resonant LWA can be achieved by using a resonant air cavity below a semi-infinite dense medium (the lens), as displayed in Fig. 1. When comparing the radiation of a LWA into a semi-infinite medium with a dense permittivity ε_r to a standard LWA with a partially reflecting surface radiating into free space, both antennas present the same propagation constants and therefore the same effective area, A_e. However, the LWA radiating into a dense medium achieves a ε_r-times higher directivity since the directivity is $4\pi A_e \varepsilon_r/\lambda_0^2$, where λ_0 is the wavelength at the center frequency f_0. One of the implications of this enhanced directivity is that the far-field region will be at a much further distance.

To illustrate this effect, we analyze the near field of the geometry shown in Fig. 1, consisting of a source located in an infinitely extended ground plane and a lossless semi-infinite dielectric medium with relative permittivity $\varepsilon_r = 11.9$ (silicon) separated by a $h = \lambda_0/2$ air cavity. The origin of the reference system is taken at a distance Δz below the ground plane, since it is known that these kinds of leaky-wave antennas have the phase center below the ground plane [30]. The electric field at observation point $\vec{r}(\rho, \phi, z)$, located in the semi-infinite silicon, can be evaluated by resorting to a spectral Green's function representation [32]. The electric field radiated in the

infinite medium by a magnetic current source located in the ground plane and, without loss of generality, oriented along $\hat{y}$ can be expressed as

$$\vec{e}(\vec{r}) = \frac{1}{4\pi^2}\int_0^{\infty}\int_0^{2\pi} \tilde{G}^{em}(k_\rho,\alpha)M(k_\rho,\alpha)\hat{y} \cdot e^{-jk_\rho\rho\cos(\alpha-\phi)}e^{-jk_z z}k_\rho \mathrm{d}\alpha \mathrm{d}k_\rho \quad (1)$$

with $\tilde{G}^{em}(k_\rho,\alpha)$ being the dyadic spectral Green's function for stratified media that gives the electric field at the top of the air cavity due to a magnetic current source, $k_z = (k_d^2 - k_\rho^2)^{1/2}$ with $k_d = k_0\sqrt{\varepsilon_r}$ the wavenumber in the infinite medium and $M(k_\rho,\alpha)$ the Fourier transform of the equivalent magnetic current of the source. The cylindrical spectral coordinates are given from the cartesian spectral coordinates by the transformation $k_x = k_\rho\cos\alpha$ and $k_y = k_\rho\sin\alpha$ and the cylindrical spatial coordinates are given by the transformation $x = \rho\cos\phi$, $y = \rho\sin\phi$, respectively. The spectral Green's function can be expressed as a function of the forward voltage $V^+_{TM/TE}$ solution in the infinite medium at the air–dielectric interface of the corresponding transmission line problem as follows [32]:

$$\tilde{G}^{em}(k_\rho,\alpha) = V^+_{TE}\hat{\alpha}\hat{k}_\rho - V^+_{TM}\hat{k}_\rho\hat{\alpha} + \frac{k_\rho}{k_z}V^+_{TM}\hat{z}\hat{\alpha} \quad (2)$$

where $\hat{k}_\rho = (k_x\hat{x} + k_y\hat{y})/k_\rho$ and $\hat{\alpha} = (k_x\hat{y} - k_y\hat{x})/k_\rho$. To make the dependence of the phase center explicit, one can consider the spectrum of the electric field assuming the origin of the reference system centered at the ground plane wherein the source is located, $V^+_{TM/TE}(k_\rho, \Delta z = 0)$, and construct the following auxiliary functions:

$$\tilde{V}^+_{TM/TE}(k_\rho,\Delta z) = V^+_{TM/TE}(k_\rho,\Delta z = 0)e^{-jk_z\Delta z} \quad (3)$$

so that integrand in (1) now contains $\tilde{G}^{em}(k_\rho,\alpha)e^{-jk_\rho\rho}e^{-jk_z z'}$, where $z' = z + \Delta z$.

For an elementary source, the α-integral can be closed analytically into Hankel functions, where $H_n^{(2)}$ are Hankel functions of the second kind with order n, such that only the k_ρ-integrals remain [24]–[26]. For a distributed source, similar steps can be taken for observation points far from the source when the spectral current $M(k_\rho,\alpha)$ can be assumed to be slowly varying in α compared to $\tilde{G}^{em}$ and can therefore be evaluated in the α-saddle point, i.e., $M(k_\rho,\phi)$. The complete $\vec{e}(\vec{r})$ and $\vec{h}(\vec{r})$ expressions given in Appendix A are then of the form

$$\int_{-\infty}^{\infty} V^+_{TM/TE}H_n^{(2)}(k_\rho\rho)M(k_\rho,\phi)e^{-jk_z z}k_\rho dk_\rho \quad (4a)$$

with $n = \{0, 2\}$ or

$$\int_{-\infty}^{\infty} I^+_{TM}H_1^{(2)}(k_\rho\rho)M(k_\rho,\phi)e^{-jk_z z}k_\rho^2 dk_\rho. \quad (4b)$$

When the observation point is in the far-field of the LWA, an asymptotic evaluation in both saddle points for $k_\rho = k_d\sin\theta$ and $\alpha = \phi$ can be done arriving to the following expression:

$$\vec{e}(\vec{r}_\infty) \approx jk_d\left(-\hat{\theta}V^+_{TM}\cos\phi + \hat{\phi}V^+_{TE}\cos\theta\sin\phi\right) \times M(k_\rho,\alpha)\frac{e^{-jkr}}{4\pi r}. \quad (5)$$

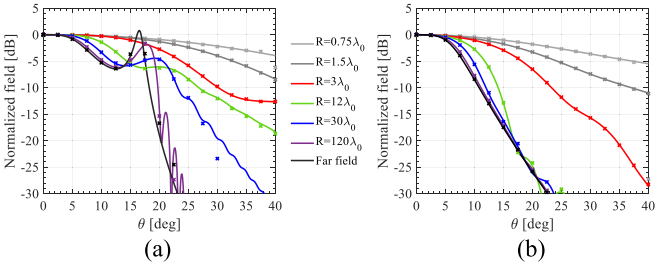

Fig. 2. Electric fields in the (a) E-plane ($\hat{\theta}$ component) and (b) H-plane ($\hat{\phi}$ component) radiated by a $\hat{y}$-oriented elementary magnetic current source evaluated over a spherical region with radius R from the source (i.e., $\Delta z = 0$). Solid lines: (5), crosses: CST.

As a first example, let us consider an elementary magnetic current source with the reference system located in the source as most cases in the literature [26], [27]. The $\hat{\theta}$-component of the electric field in the E-plane radiated by this source into the semi-infinite (silicon) medium is shown in Fig. 2(a). The electric field has been calculated using (1) over several spherical cuts in the E-plane with radii R between $0.75\lambda_0$ and $120\lambda_0$ centered at the origin (the spheres are shown as dashed lines in Fig. 1). For reference, the far-field approximation of (5) is also shown. We can observe that the shape of the near fields shown in Fig. 2 is strongly dependent on R and converges to the far field only at very large distances from the source. This is due to the TM_0 modal field that dominates the field in the angular region close to the complex pole location even for very large R. Furthermore, the radiation patterns are asymmetric in ϕ, since the TM_0 mode does not radiate in the H-plane. Therefore, to efficiently feed electrically small silicon lenses, it is clear that the TM_0 mode must be suppressed, for example, by using a double-slot iris [7], [11], [33], [34] or dipole source configurations [35]. To illustrate the accuracy of (1), the obtained fields are compared to those obtained from the time-domain solver of CST [36], a commercial full-wave solver. Open boundary conditions were applied to an elementary source or a double-slot iris radiating into a semi-infinite structure made of the considered dielectric materials.

The fields radiated into the same stratification as above but now for the double-slot iris source with the same dimensions as in [7] are shown in Fig. 3(a) and (b), taking again the coordinate reference system located at the center of the double slot. The inset of Fig. 3(b) shows the geometry of the double-slot iris and the dimensions are given as $\alpha_i = 100°$, $\rho_i = 0.55\lambda_0$ and $w_i = 0.15\lambda_0$ [7]. The near field is calculated over the same spherical regions as for the elementary source in Fig. 2, again using (1) (solid lines) and full-wave simulations (crosses) to validate the fields. The small discrepancy at the closest distances comes from the approximation of the spectral current $M(k_\rho,\alpha) \approx M(k_\rho,\phi)$. At distances smaller than λ_0 from the double-slot source, the approximation on the α-integral is not accurate anymore. The use of a double-slot source leads to much faster convergence of the near field to the far field compared to the elementary source due to the suppression of the TM_0 mode.

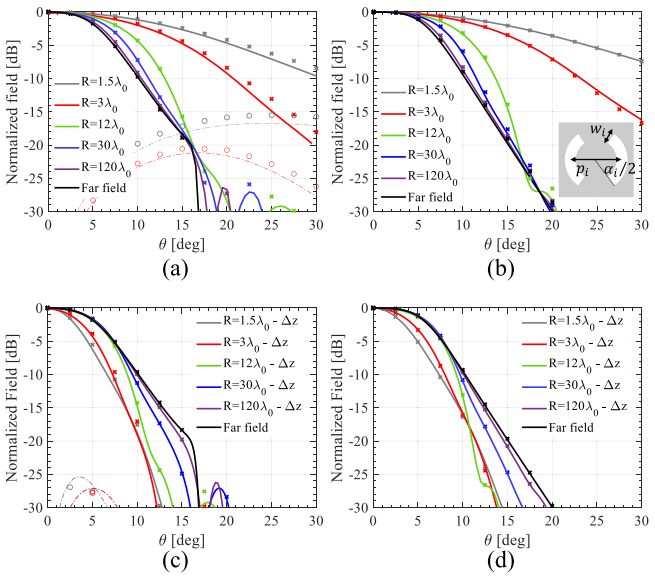

Fig. 3. Electric fields radiated by the double-slot iris of [6], evaluated over a spherical region with several radii calculated using (4): (a) E-plane ($\hat{\theta}$-component) and (b) H-plane ($\hat{\phi}$-component) amplitude seen from the slots ($\Delta z = 0$) and (c) E-plane ($\hat{\theta}$-component) and (d) H-plane ($\hat{\phi}$-component) amplitude seen from the phase center according to [30] ($\Delta z = -5.6\lambda_0$). Dashes: $\hat{r}$-component, crosses and circles: CST.

It is well known that the phase center in LWAs lies below the ground plane in the far field. In [30], the following approximate formula for the phase center, dependent only on the normalized attenuation constant of the leaky-wave pole $\hat{\alpha}_{LWi}$, was given:

$$\frac{\Delta z_i}{\lambda_0} \approx -\frac{1}{2\pi \hat{\alpha}_{LWi}^2 \sqrt{\varepsilon_r}} \tag{6}$$

where, in case of a LW radiating into a dense medium $\hat{\alpha}_{LWi} = Im\{k_\rho^{LWi}/k_d\}$ and the term $\sqrt{\varepsilon_r}$ appears in the denominator.

We can now plot the near fields of the same source considered in Fig. 3(a) and (b), but evaluated at spheres centered at this approximated phase center, which is $\Delta z = -5.6\lambda_0$ for a silicon semi-infinite medium (the spheres are shown as solid lines in Fig. 1). We can see that the amplitude converges even faster to the far-field approximation indicating that the field may be considered, also very close to the source, as a spherical wave but with a more accurate phase center evaluation. In [30], other phase-minimization formulas were also considered to improve the accuracy of (6); however, these were not closed-form and were given as a function of a generic solid angle.

To properly understand the properties of the field radiated by this kind of LWA close to the source, we will employ a spectral analysis that decomposes the total field in terms of a space wave, calculated by integration over the SDP from the phase center, and multiple leaky-wave modal fields, associated with poles that are captured by the SDP path deformation [24, p. 468] in Section III.

III. Spectral Field Decomposition of the Near Field in Resonant Leaky-Wave Antennas

In this section, we apply a spectral-domain field decomposition to the near field radiated by resonant leaky-wave antennas into a semi-infinite medium. This near field is expressed as the summation of (multiple) leaky-wave modal fields plus a space wave contribution. This latter one can be evaluated with an integration path over the branch point close-by the source as in [28] or using the SDP for larger distances [24, p. 467]. Here, in contrast to [26] and [28], we apply this SDP directly for the near-field evaluation in resonant LWAs, provided that the reference system is located in the phase center and that the near field is evaluated at a distance from the source such that the asymptotic decomposition holds (i.e., the observation point is outside the region that includes the phase center and source points).

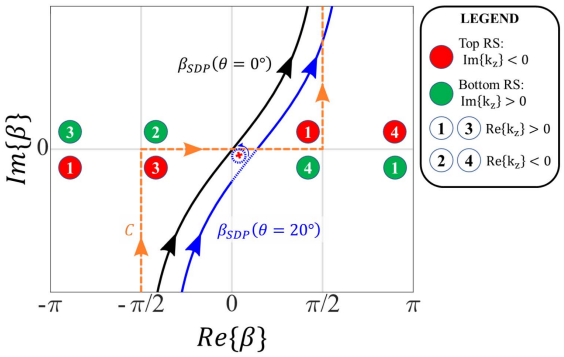

Fig. 4. SDPs β_{SDP} in the complex β-plane for observation points $\theta = 0°$ and $\theta = 20°$. The choice of Riemann sheet for the β_{SDP}-integral is indicated in the legend.

To evaluate the SDP field contribution, a change of spectral variables $k_\rho = k_d \sin\beta$, $k_z = k_d \cos\beta$ suggests using a spherical coordinate system for the observation point $\vec{r}(\theta, \phi, R)$ in (4a) and (4b) with origin in the antenna phase center, Δz. The resulting integrals are then of the form

$$\int_C V_{TM/TE}^{+} H_n^{(2)}(k_d \rho \sin\beta) \times M(k_d \sin\beta, \phi) \times e^{-jk_d z \cos\beta} k_d^2 \sin\beta \cos\beta d\beta \tag{7a}$$

with $n = \{0, 2\}$ or

$$\int_C I_{TM}^{+} H_1^{(2)}(k_d \rho \sin\beta) M(k_d \sin\beta, \phi) \cdot e^{-jk_d z \cos\beta} k_d^3 \sin^2\beta \cos\beta d\beta \tag{7b}$$

with the integration path C shown in the complex β-plane in Fig. 4. The odd- and even-numbered regions indicate $Re\{k_z\} > 0$ and $Re\{k_z\} < 0$ and the red and green regions indicate the top and bottom Riemann sheets (i.e., $Im\{k_z\} < 0$ and $Im\{k_z > 0\}$), respectively [24, p. 463].

When the original path C is deformed and no singularities are crossed, the total field $\vec{e}(r)$ is given by the integration over the deformed path. When the deformation leaves a pole between the original and the new path, the residue contribution corresponding to the pole encountered must be summed to the new path integral to obtain the total field.

It can be shown using the method in [25] that for large observation distances, i.e., where the large-argument approximation of the Hankel functions [24, p. 467] is valid, the parameterization of the SDP in (7) is achieved with a change of

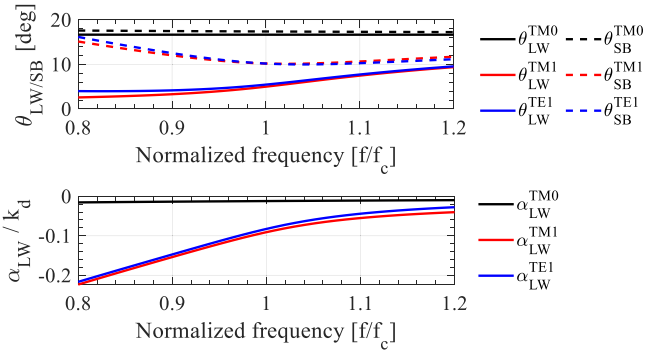

Fig. 5. Leaky-wave poles $k_{\rho,LW}^{TM/TE} = k_d(\sin\theta_{LW}^{TM/TE} + j\alpha_{LW}^{TM/TE})$ that propagate in the stratification of Fig. 1 with semi-infinite dielectric permittivity $\varepsilon_r = 11.9$ (silicon). The shadow boundary angle [see (9)] is also shown.

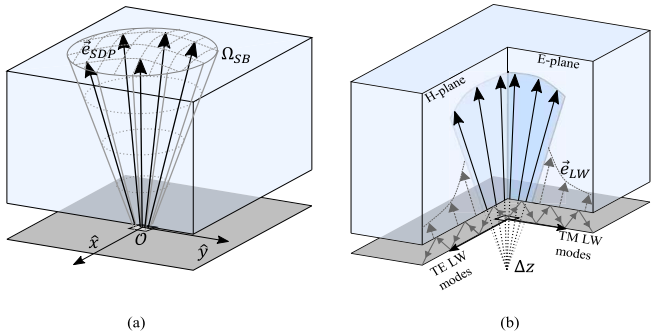

Fig. 6. Three-dimensional view of the considered LWA. (a) In the spherical cone region Ω_{SB} as seen from the phase center at Δz below the ground plane, the total field is given by $\vec{e}_{SDP}$ (solid arrows). (b) Outside this cone, the LW modal field $\vec{e}_{LW}$ (dotted arrows) must be added to the SDP contribution to obtain the total field.

variable $\beta \to \tau$ with $\tau \in [-\infty, \infty]$ and τ given by inverting

$$\beta_{SDP} = \theta + 2\,\text{asin}\left(\tau e^{j\frac{\pi}{4}}\Big/\sqrt{2}\right). \tag{8}$$

Accordingly, this contribution, when evaluated asymptotically, will give rise to a dominant spherical wave emerging from the phase center. From Fig. 4, one can note that the path of the SDP includes portions in the bottom Riemann sheet, and thus the poles encountered are leaky-wave poles and we call the residue contribution of these poles the leaky-wave modal field $\vec{e}_{LW}(\vec{r})$.

The leaky-wave poles $k_{\rho,LW}^{TM/TE}$ arise from the denominator of $V_{TM/TE}^{+}$ in (4). They may be found by solving the appropriate dispersion equation (or by using approximated analytical expressions [37]). They are conveniently represented as $k_{\rho,LW}^{TM/TE} = k_d(\sin\theta_{LW}^{TM/TE} + j\alpha_{LW}^{TM/TE})$: $\theta_{LW}^{TM/TE}$ is the leaky-wave pointing angle and $\alpha_{LW}^{TM/TE}$ is the leakage rate [1] of the TM or TE pole. The stratification of Fig. 1 supports three leaky-wave modes: TM_0, TM_1, and TE_1, with their propagation constants shown in Fig. 5 as a function of frequency.

The SDP crosses a TE or TM leaky-wave pole when $\theta \geq \theta_{SB}^{TM/TE}$, i.e., when the observation point lies below the corresponding shadow boundary, see Fig. 1. The shadow boundary angle is a function of the pole's complex propagation constant as follows [24, p. 468, 25]:

$$\theta_{SB}^{TM/TE} = \text{Re}\left\{\beta_{LW}^{TM/TE}\right\} + \text{acos}\left(\text{sech}\left(\text{Im}\left\{\beta_{LW}^{TM/TE}\right\}\right)\right) \tag{9}$$

in which $\beta_{LW}^{TM/TE} = \text{asin}(k_\rho^{LW}/k_d)$. This shadow boundary angle is also shown as a function of frequency in Fig. 5 for each of the leaky wave poles present. It is clear that $\theta_{SB}^{TM/TE}$ is not close to the corresponding $\theta_{LW}^{TM/TE}$, except for the TM_0 mode, which does not enhance the broadside directivity of the antenna, as explained in Section II.

If multiple leaky-wave poles are crossed, the total field is given by adding the modal fields associated with each crossed pole to the contribution from the SDP

$$\vec{e}(\vec{r}) = \vec{e}_{SDP}(\vec{r}) + \sum_{i=1}^{m} \vec{e}_{LW}^{TM/TE}(\vec{r})\Big|_{\theta \geq \theta_{SB}^{TM/TE}} \tag{10}$$

as long as the observation point is outside the elliptical transition region [25] and the LW poles are not close together. Expressions for $\vec{e}_{LW}^{TM/TE}(\vec{r})$ may be found in Appendix B. The LW modal field is a cylindrical wave that propagates in the $\theta_{LW}^{TM/TE}$-direction (see Fig. 5) in the infinite medium. Therefore, this field decomposition indicates that the total field could only be represented by a spherical wave until the shadow boundary when $\vec{e}_{SDP}$ dominates. The field representation of (10) in terms of an SDP contribution and LW modal field contribution is shown in Fig. 6. The origin of this spherical wave will be at the phase center of the antenna, Δz, which will be evaluated in Section IV.

IV. Phase Center Evaluation

The phase center in the considered resonant LWAs can be defined for the near field, similar to the far field, as the apparent origin of radiation such that the phase of the integrals in (4) is minimized over a certain solid angle. Based on the understanding that the near field could only be a spherical wave when $\theta < \theta_{SB}$ (see Section III), the solid angle over which to minimize this can be given as $\Omega_{SB}(\theta, \phi)$ such that $\theta \in [0, \theta_{SB}]$ and $\phi \in [0, 2\pi]$, instead of a generic angle as in [30]. Since the considered LW antennas are nearly rotationally symmetric (with similar TE_1/TM_1 modes), the location of the phase center will be along the z-axis. The phase in (4) is dominated by the phase of the transmission-line voltage solutions, $V_{TM/TE}^{+}$. In [30], an approximated expression of this phase is given using only the LW propagation constant.

To find the most appropriate value Δz that guarantees the path deformations in Fig. 4 correspond to the SDP, one can consider a nonuniform asymptotic evaluation of the integral in (4). The integral can be deformed into an SDP and recognized as a spherical wave, if the kernel, now (3), separated from the exponential oscillating phase associated with the observation point in (2) is slowly varying. Expressing $k_\rho = k_d \sin\beta$, the normalized phase of $\tilde{V}_{TM/TE}^{+}(k_\rho, \Delta z)$ can be expressed as a function of β as [30]

$$\tilde{\Psi}(\beta, \Delta z) = \text{atan}\left(\sin^2\beta\big/2\alpha_{LW}^2\right) - k_d \Delta z \cos\beta. \tag{11}$$

In Fig. 7(a), $\tilde{\Psi}(\beta, \Delta z)$ is shown for a silicon medium and $\Delta z = 0$ together with the phase of $e^{jk_z\Delta z}$ when $\Delta z = -3.2\lambda_0$. It can be seen from the figure that the two phases are

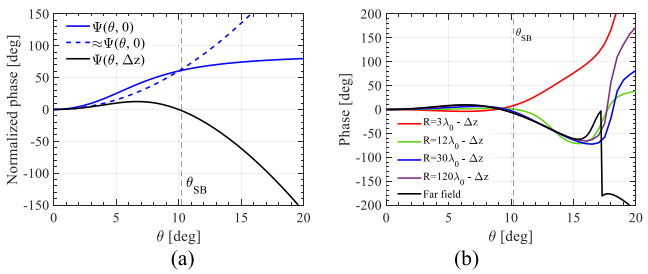

Fig. 7. (a) Phase $\Psi(\theta, \Delta z = 0)$ of (3) along with its approximation (blue). The corrected phase for the phase center of (13) $\Psi(\theta, \Delta z = -3.2\lambda_0)$ is also shown (black). The shadow boundary angle is indicated. (b) Phase of the E-plane near field radiated by the LWA with a double-slot iris, evaluated at different radii from the phase center $\Delta z = -3.2\lambda_0$.

very similar until the shadow boundary angle θ_{SB}. Therefore, we can evaluate the phase center $\Delta z^{TM/TE}$ associated with the TM and TE poles by imposing that the two functions are equal at the shadow boundary for each of the poles

$$\Psi\left(\theta_{SB}^{TM/TE}, \Delta z = 0\right) = k_{\mathrm{z,SB}}^{TM/TE} \Delta z^{TM/TE} \tag{12}$$

where $k_{\rho,\mathrm{SB}}^{TM/TE} = k_d \sin\theta_{SB}^{TM/TE}$. Solving this equation, a good evaluation of the phase center per pole can be given by

$$\frac{\Delta z^{TM/TE}}{\lambda_0} = -\frac{\operatorname{atan}\left(\sin^2\theta_{SB}^{TM/TE} \Big/ 2\left(\alpha_{LW}^{TM/TE}\right)^2\right)}{\sqrt{\varepsilon_r} 2\pi\left(1 - \cos\theta_{SB}^{TM/TE}\right)} \tag{13}$$

in which a negative $\Delta z^{TM/TE}$ refers to a phase center position below the ground plane. In general, the TM pole will give the E-plane phase center and the TE pole will give the H-plane phase center. For high dielectric contrast cases, $k_{\rho,LW}^{TM} \approx k_{\rho,LW}^{TE}$ [30] leads to nearly overlapping E- and H-plane phase centers at Δz. For example, the phase center of the silicon LWA described previously is $\Delta z = -3.2\lambda_0$ when the TE and TM solutions are averaged. The validity of this equation is shown in Fig. 7(b) where the E-plane phase radiated by the LWA fed by a double-slot iris is indeed nearly constant for $\theta < \theta_{SB}$ when the reference system is taken to coincide with the phase center given by (13).

With the phase center definition of (13), a uniform asymptotic expansion of the integral in (4) over the SDP can be derived using the approach in [25]. Such a uniform asymptotic expansion results in a contribution from a Fresnel-type transition function in an elliptical region around the phase center. The equality of the phase of the space wave and the leaky-wave modal fields, which have spherical and cylindrical spreading, respectively, at the shadow boundary imposed by the phase center definition in (13), leads to the smallest possible dimension of the elliptical transition region.

V. Spherical Wave Near-Field Representation for Resonant LWAs

In this section, the formation of a spherical wave in a certain solid angle around broadside in the near field of resonant LWAs is investigated based on the previous spectral field decomposition. In Section V-A the analysis is performed for high-permittivity (silicon) lenses and in Section V-B the analysis is performed for low-permittivity (plastic) lenses. Finally, in Section V-C, the leaky-wave poles, shadow boundary angle, and phase center are presented as a function of the permittivity of the infinite medium ($2 \le \varepsilon_r \le 12$).

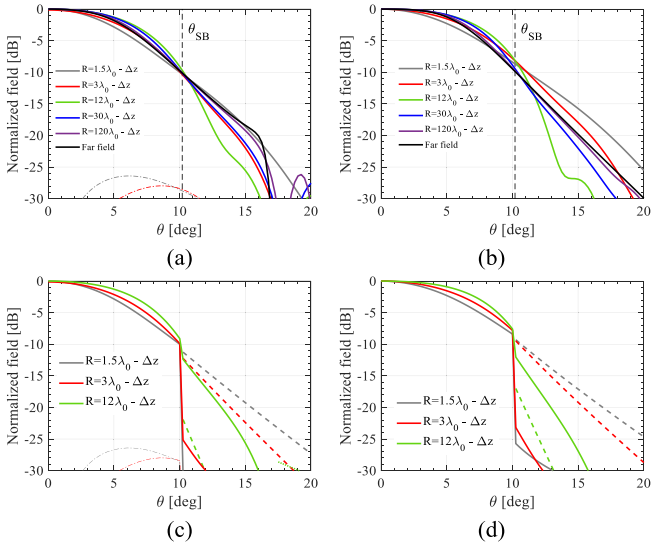

Fig. 8. Electric fields in the (a) E-plane ($\hat{\theta}$ component and $\hat{r}$ component) and (b) H-plane ($\hat{\phi}$ component) radiated by the double-slot iris of [7], evaluated over a spherical region with several radii taken from $\Delta z = -3.2\lambda_0$, i.e., below the ground plane. The shadow boundary angle of (9) is indicated. The decomposition into the SDP contribution (solid lines) and LW modal fields (dashes: main modes, dots: TM0 mode) are shown in (c) E-plane and (d) H-plane.

A. High Dielectric Contrast: Silicon Lenses

The fields of the double-slot iris-fed LWA are calculated using (10) over spheres centered at the phase center, as defined by (13) with the aim of understanding the behavior of the field amplitude, polarization, and propagation direction. The radius of the spheres is chosen between $1.5\lambda_0 - \Delta z$ and $120\lambda_0 - \Delta z$ so that the spheres have coincident observation points at broadside with those of Fig. 3. The resulting E- and H-plane near fields are shown in Fig. 8(a) and (b). The near field, when evaluated from the phase center, is almost independent of the distance from the source in the region $\theta < \theta_{SB}$. In Fig. 8(c) and (d) we show the field decomposition into the space wave evaluated using the SDP and the leaky-wave terms. The influence of the TM_1 and TE_1 leaky-wave modal fields is observed when $\theta > \theta_{SB}$, at which point the field level is already below -10 dB. The radial field component diminishes very rapidly with R and is already below -25 dB at $R = 1.5\lambda_0 - \Delta z$.

Since the phase over the SDP is nearly constant, the space-wave evaluation can be approximated using a nonuniform asymptotic expansion of the SDP integral, which corresponds to the far-field given in (5)

$$\vec{e}_{SDP}(\vec{r})|_{\theta<\theta_{SB}} \approx \vec{e}(\vec{r}_\infty, \Delta z)|_{\theta<\theta_{SB}} \tag{14}$$

where it is highlighted that this applies only with a proper phase center definition. The far-field is also shown in Fig. 8.

This nonuniform asymptotic evaluation can be considered sufficiently accurate to describe the SDP field until θ_{SB} because the field level at the shadow boundary is already very low (i.e., about -10 dB in Fig. 8). This is due to the fact that the geometry considered in this article supports two $\pm k_{\rho LW}$ leaky waves that cumulatively provide a maximum at broadside, and a decreasing total field already for observation points close to the shadow boundaries. For other configurations where the shadow boundary would correspond to higher field levels, a uniform asymptotic evaluation as in [25] would be needed to maintain useful accuracy. The phase in Fig. 7(b) varies by less than 10° in the region $\theta < \theta_{SB}$ for any R and can thus the near field can be considered a spherical wave. Since this angle also corresponds to the -10 dB point of the radiation pattern, the lens' subtended solid angle, seen from the phase center, can be approximated by Ω_{SB}. This solid angle in (9) and phase center in (13), which are only a function of the propagation constant of the LW mode, fully define the shape of the lens needed to enhance the directivity in this kind of antennas as shown in the next section.

To illustrate that the field close to the LW source can be well represented by a spherical wave, a 2-D cut of the real part of the electric field in the E-plane is shown in Fig. 9(a), which has been obtained from a full-wave simulation. It is clear from this figure that there is a spherical wavefront in the semi-infinite medium, even very close to the air-dielectric interface. Next, the direction of time-averaged power flow has been calculated from the Poynting vector $\vec{S} = \mathrm{Re}\{\vec{e} \times \vec{h}^*\}/2$ in the E-plane seen from the phase center. This direction is shown in Fig. 9(c) and is compared to the geometrical radial vector. Indeed, when the near field is evaluated from the phase center, the Poynting vector is almost along $\vec{r}$, which confirms that the near field may be considered a local spherical wave in the region $\theta < \theta_{SB}$ and that it will couple well to an elliptical lens, even for electrically small lenses.

We can also evaluate the fraction of power in the space wave by integrating the Poynting vector over the solid angle Ω_{SB}

$$P_{\mathrm{rad}}(R) = \iint_{\Omega_{SB}} \frac{1}{2} Re\left\{\vec{e}_{SDP} \times \vec{h}^*_{SDP}\right\} \cdot \hat{r} R^2 d\Omega. \qquad (15)$$

The ratio of this power to the total radiated power by the LWA, i.e., $P_{\mathrm{rad}}(R)/P_{tot}$, will correspond to the spillover efficiency of the truncated lens. In Fig. 10, this spillover efficiency is shown as a function of the lens diameter $D = 2R\sin\theta_{SB}$. From this result, we can see that the spillover efficiency is higher than 85% for lenses larger than $D = 2\lambda_0$. Thus, depending on the specific requirements, silicon lenses as small as $D_l = 2.5\lambda_0$ can be used. When the double-slot iris is omitted, and thus the TM0 mode is present, the lens size must be significantly larger in order to achieve the same efficiency.

B. Low Dielectric Contrast: Plastic Lenses

The use of low-permittivity lenses, which have LW poles that are much further from the real axis, has recently been proposed to achieve a very wide bandwidth of 40% [11].

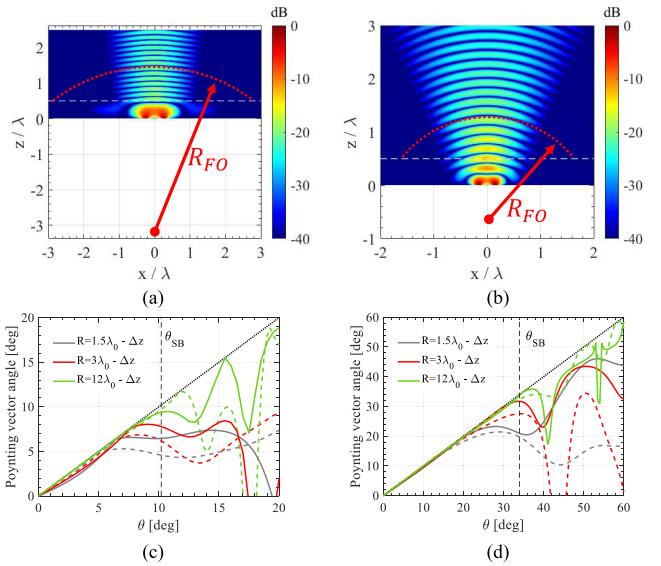

Fig. 9. Two-dimensional E-plane cut of the field radiated by the double-slot iris source into an (a) silicon and (b) plastic semi-infinite medium. Poynting vector angle (solid: E-plane, dashes: H-plane) for the fields in (c) silicon (see Fig. 8) and (d) plastic (see Fig. 12). The black dotted line indicates the geometrical angle seen from the phase center.

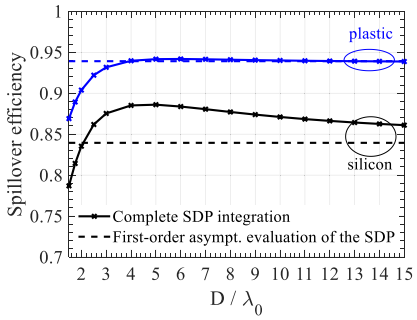

Fig. 10. Spillover efficiency as a function of the lens diameter.

The stratification is the same as considered before (see Fig. 1), except the semi-infinite silicon is replaced with HDPE ($\varepsilon_r = 2.5$, considered lossless here), a low-cost plastic commonly used in mm-wave applications. The proposed lens feed is a waveguide-fed double-slot iris, similar to [11], with dimensions $\alpha_i = 120°$, $\rho_i = 0.6\lambda_0$ and $w_i = 0.2\lambda_0$, designed to suppress the TM0 mode. The leaky-wave propagation constants are shown in Fig. 11 as a function of frequency, along with the resulting shadow boundary angle. Note again that θ_{SB} is very far from θ_{LW} for the main $\mathrm{TM}_1/\mathrm{TE}_1$ modes and that they are nearly equal for both modes. Since the main LW poles are not as close together as in the silicon case, the phase center $\Delta z = -0.64\lambda_0$ has been calculated by averaging (13).

The field radiated by this source into the semi-infinite medium, $\vec{e}$, has been calculated using (10) over several spherical cuts in the E-plane with radii R between $1.5\lambda_0 - \Delta z$ and $12\lambda_0 - \Delta z$, centered at the phase center. For reference, the far field is also shown. The result is shown in Fig. 12(a) and (b) (solid lines). The field is again not strongly dependent on R. In Fig. 12(c) and (d) the field is decomposed into the

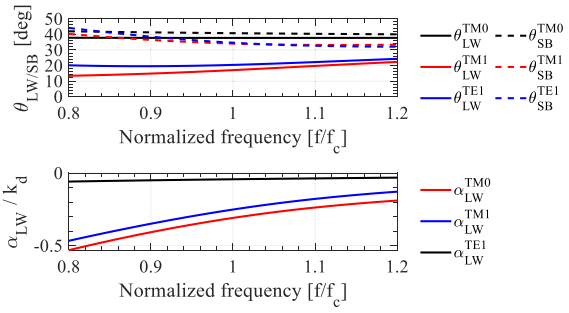

Fig. 11. Leaky-wave poles $k_\rho^{LWP} = k_d(\sin\theta_{LW} + j\alpha_{LW})$ that propagate in the stratification of Fig. 1with semi-infinite dielectric permittivity $\varepsilon_r = 2.5$ (plastic). The shadow boundary angle [see (9)] is also shown.

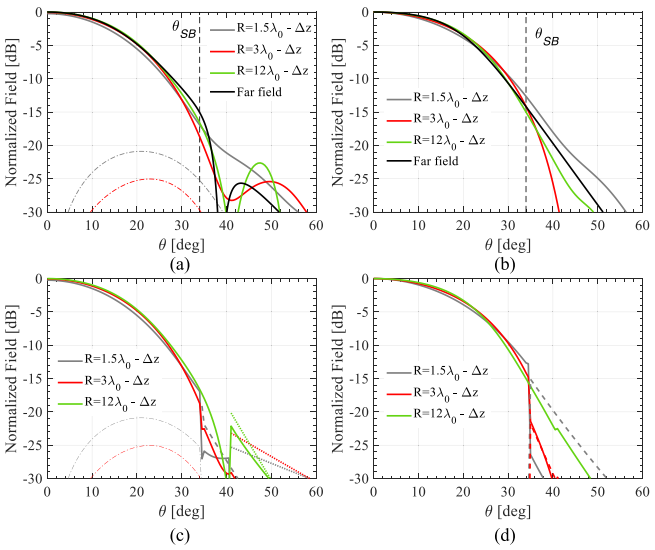

Fig. 12. Electric fields in the (a) E-plane ($\hat{\theta}$ component and $\hat{r}$ component) and (b) H-plane ($\hat{\phi}$ component) radiated by the double-slot iris of [11], evaluated over a spherical region with several radii taken from $\Delta z = -0.64\lambda_0$, i.e., below the ground plane. The shadow boundary angle of (9) is indicated. The decomposition into the SDP contribution (solid lines) and LW modal fields (dashes: main modes, dots: TM_0 mode) are shown in (c) E-plane and (d) H-plane.

contributions from $\vec{e}_{SDP}$ (solid lines) and $\vec{e}_{LW}$ (dashes and dots), which sum to $\vec{e}$ [see Fig. 12(a) and (b)]. The discontinuity in $\vec{e}_{SDP}$ is due to the SDP crossing the LW pole.

To illustrate that the near field can be considered a local spherical wave, a 2-D cut of the near field is shown in the E-plane in Fig. 9(b). Furthermore, the angle between the time-averaged Poynting vector $\vec{S}$ and the radial direction, seen from the phase center, is shown in Fig. 9(d). It is clear that the field can be considered a local spherical wave for $\theta < \theta_{SB}$ even for observation points close to the source. Thus, the approach can be used for stratifications that are less resonant than in Section V-A and much less resonant than previously described in the literature [26].

VI. Application to Small Elliptical Lenses

In this section, the geometry of the elliptical lens fed by the resonant leaky-wave feed with a double-slot iris is given analytically, based on the SDP field decomposition,

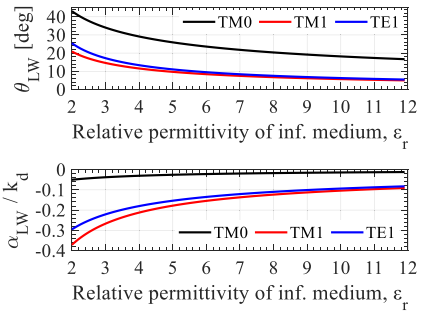

Fig. 13. Leaky-wave pointing angles θ_{LWi} and normalized attenuation constants $\hat{\alpha}_{LWi}$ at the central frequency as a function of the permittivity of the infinite medium.

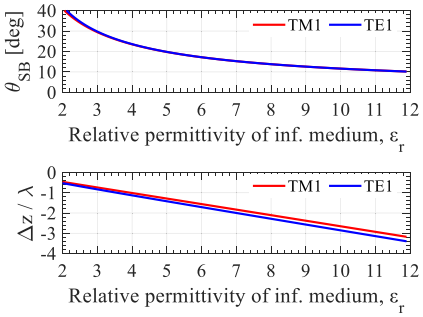

Fig. 14. Shadow boundary angle θ_{SB} and phase center Δz corresponding to the main modes as a function of the permittivity of the infinite medium.

for arbitrary lens permittivity. The formulas provided can be used to design the lens geometry even in the near field with high aperture efficiency. We apply an FO methodology in reception [11], [31] to calculate the aperture efficiency and the radiation patterns of a small silicon lens, which are verified using full-wave simulations. The aperture efficiency is then calculated as a function of the lens diameter D_l.

A. Spherical-Wave Parameters for Arbitrary Dielectric Contrast

To define the geometry of an elliptical lens antenna, we must know θ_{SB} and Δz for the desired lens permittivity. Therefore, we present here the LW poles as a function of the permittivity of the semi-infinite dielectric medium, ε_r. These are then used to derive θ_{SB} and Δz as a function of ε_r.

The leaky-wave pointing angle θ_{LW} and leakage rate $\hat{\alpha}_{LW}$ are shown in Fig. 13 as a function of the relative permittivity of the semi-infinite medium. The LW angle decreases and the leakage is slower as the permittivity increases, which is in line with the results for the classical Fabry–Pérot antenna geometry [1], [37].

The shadow boundary angle θ_{SB} and phase center location for the main TM_1 and TE_1 modes, calculated using (9) and (13), are shown in Fig. 14 as a function of the relative permittivity of the semi-infinite medium. The shadow boundary angles are almost equal for both modes and decrease with an increasing ε_r. The phase center is further below the ground plane as ε_r increases. Together, the shadow boundary angle and phase center location fully define the elliptical

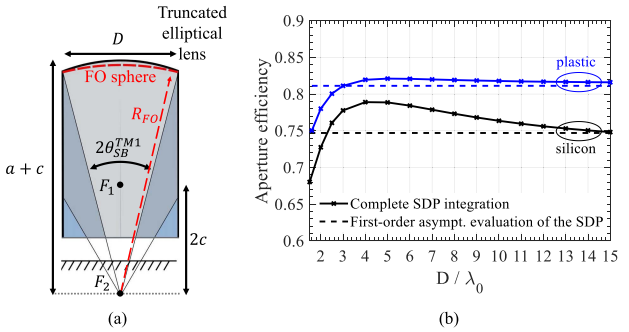

Fig. 15. (a) Cross section of an elliptical lens fed by the stratification of Fig. 1 with the foci and dimensions of the ellipse and lens. (b) Aperture efficiency of the analytical lens geometry of (a) based on the leaky modes as a function of the lens diameter.

lens geometry to which the LWA couples well, as will be demonstrated next.

B. Elliptical Lens Geometry

The analytical elliptical lens geometry that provides high aperture efficiency [see Fig. 15(a)] is as follows. The lower focus of the ellipsoid, F_2, coincides with the phase center Δz of the feed given by (13) and the lens is truncated at an angle θ_{SB}, given by (9), seen from this focus since the shadow boundary angle corresponds roughly to the -10 dB field taper angle. The values for Δz and θ_{SB} can be found in Fig. 14. The distance from F_2 (i.e., the phase center) to the rim of the lens is $R_{FO} = D_l/(2\sin\theta_{SB})$. The sphere centered at F_2 with radius R_{FO} is the FO sphere. The semi-major axis of the ellipsoid is given by

$$a = R_{FO}(1 - e\cos\theta_{SB})\big/\left(1 - e^2\right) \tag{16}$$

and the inter-focal distance is given by $c = a \cdot e$, where $e = 1/\sqrt{\varepsilon_r}$ is the eccentricity of the lens.

C. Lens Analysis in Reception

To calculate the aperture efficiency of the lens, we use the FO method in reception [31], which we briefly summarize here. In the FO approach, a plane wave incident on the lens in the $\hat{k}^i = -\hat{z}$ direction is propagated into the lens and onto the FO sphere (S_{FO} with normal $\hat{n} = -\hat{r}$ pointing inward) using geometrical optics (GO). The equivalent electric and magnetic currents on the FO sphere $\vec{J}^{\,\mathrm{eq}}_{S_{FO}} = \hat{n} \times \vec{h}^{\,GO}_{S_{FO}}$ and $\vec{M}^{\,\mathrm{eq}}_{S_{FO}} = -\hat{n} \times \vec{e}^{\,GO}_{S_{FO}}$ are then correlated with the SDP contribution to the near field of the leaky-wave feed, $\vec{e}_{SDP}(\vec{r})$ and $\vec{h}_{SDP}(\vec{r})$, as follows:

$$P_L(\hat{k}_i) = \frac{R_{FO}^4}{16 P_{tot}} \cdot \left| \iint_{\Omega_{SB}} \left(\vec{h}_{SDP} \cdot \vec{M}^{\,\mathrm{eq}}_{S_{FO}}(\hat{k}_i) - \vec{e}_{SDP} \cdot \vec{J}^{\,\mathrm{eq}}_{S_{FO}}(\hat{k}_i) \right) dA \right|^2 \tag{17}$$

and the aperture efficiency is given as $\eta_{ap} = P_L/P_{PW}$, where $P_{PW} = |E_{PW}|^2 \pi D_l^2/(8\zeta_0)$ and $|E_{PW}|$ is the amplitude of the incident plane wave. Since we know from Section V that the field can be modeled by a local spherical wave until the lens angle, the magnetic field is given by $\vec{h}_{SDP}(\vec{r}) = \hat{r} \times \vec{e}_{SDP}(\vec{r})/\zeta_d$ and we can simplify the correlation integral in (17) to $2\iint_{\Omega_{SB}} (\vec{e}_{SDP} \cdot \vec{e}^{\,GO}_{S_{FO}}(\hat{k}_i))dA$, which is the integral given in [11]. However, we emphasize that this approximation is only valid when the lower focus F_2 coincides with the phase center of the feed. The main novelty here is that the FO sphere is in the near field of the LW feed, where only the SDP field contribution is needed to evaluate the radiation properties of the lens-coupled LWA. Combining the FO approach with this spectral field decomposition is computationally very fast.

D. Leaky-Wave Antenna Performance

The aperture efficiency of silicon lenses has been calculated for lens diameters between $D = 1.5\lambda_0$ and $D = 15\lambda_0$ with a truncation angle θ_{SB} and phase center Δz given by (9) and (13), respectively. The rest of the lens dimensions are derived as described above. The lenses are fed by the double-slot iris of [7] and have a quarter-wave anti-reflection coating with a permittivity of $\varepsilon_{\mathrm{AR}} = 3.45$. The resulting aperture efficiency is shown in Fig. 15(b). The highest aperture efficiency is obtained when $D = 4\lambda_0$ and is almost 80%. For comparison, the field over the FO sphere has also been calculated using the far-field approximation of (14), which corresponds to making a uniform asymptotic evaluation of the SDP integral. It can be seen that the aperture efficiency of the proposed lens geometry varies less than 5% as a function of the diameter with respect to the numerical evaluation of the SDP integral.

The bandwidth achieved by such silicon LW lens antennas is in the order of 15% [7]. A larger bandwidth, around 40%, can be achieved by using a lower permittivity lens [11]. The aperture efficiency of a plastic ($\varepsilon_r = 2.5$) lens at the central frequency is shown in Fig. 15(b), where the elliptical lens' geometry has been obtained from the phase center and shadow boundary angle as described as above. The aperture efficiency of a LW-fed plastic lens is above 80% when the lens diameter is larger than $2.5\lambda_0$. The plastic lens achieves a higher aperture efficiency than the silicon lens because there is a better matching of the leaky-wave feed far-field to the incident GO field [11].

Depending on the source and lens diameter, a fine tuning of the lens parameters could lead to a slight increase of aperture efficiency. However, compared to the full-wave approach to the optimization of the phase correcting structure that have been presented in the literature [12], the fine tuning of the lens parameters here could also be achieved by using the SDP and FO approach, significantly decreasing the required optimization time.

The radiation patterns of the $D_l = 4\lambda_0$ silicon lens fed by the LW feed have been calculated using the same FO method in the near field described above, by varying $\hat{k}_i$ as explained in [17]. The radiation patterns of this lens are shown in Fig. 16, along with a full-wave simulation of the lens. The match between the patterns obtained with the FO methodology (black) and CST results (red) is excellent, especially in the main beam. The sidelobe level differs at most by 1 dB. The directivity of this lens antenna is 21 dBi.

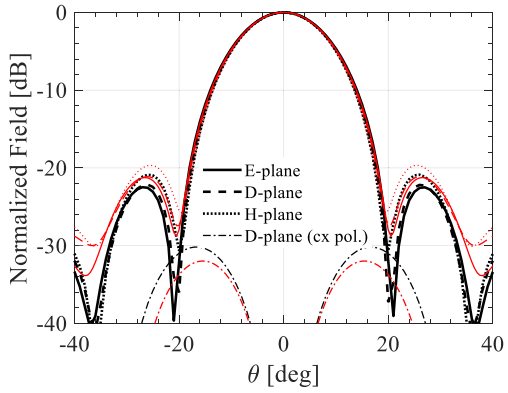

Fig. 16. Radiation pattern from a silicon lens with diameter of $D_l = 4\lambda_0$ fed by the LW stratification of Fig. 1 and double-slot iris from [7]. Black: SDP-FO method, red: full-wave simulations.

The performance of this single lens indicates we can efficiently feed lenses as small as $4\lambda_0$, which is very relevant for communication [17], [35], [38] and space [10], [16] arrays that are not fully sampled. Moreover, the achieved performances of a lens design based only on the complex propagation constant provides higher aperture efficiency than other numerically optimized phase correcting structures or shielded cavity-based LWAs [10], [12]–[14].

VII. Conclusion

In this work, we have shown that the near field of resonant LWAs radiating into a semi-infinite dielectric medium can be locally represented as a spherical wave in a certain solid angle around broadside from the phase center far below the ground plane. The near field in this solid angle can be efficiently evaluated using the integration of the spectral Green's function along the SDP, which can be approximated by a nonuniform evaluation, even very close to the LW cavity. Beyond this solid angle, defined as the shadow boundary angle, a contribution due to the leaky-wave pole must also be considered to fully describe the near field. It is shown that the complex LW propagation constants and the shadow boundary angle can be used to define the properties of the spherical wave formation accurately even in low-contrast LW cases. Therefore, the physical insight gained in this analysis can be extended to other resonant LWAs made with different kinds of stratifications such as FSS-based cases.

To demonstrate the applicability of the proposed study, we apply the understanding of the near-field spherical wave formation to the design and analysis of small- to medium-sized lenses. It is shown that the LW complex propagation constants can be used to define a truncated lens geometry that couples well to the leaky-wave antennas and achieves a high aperture efficiency for any diameter. Moreover, we have combined the SDP calculation with an FO methodology in reception to efficiently calculate the aperture efficiency and radiation patterns of such lenses. A truncated silicon lens design with a diameter of only 4 free-space wavelengths is presented that achieves almost 80% aperture efficiency. Excellent agreement with full-wave simulations is achieved, which demonstrates the accuracy of the SDP-FO methodology.

Appendix A

The field expressions for the electric and magnetic field components along $\hat{\rho}$, $\hat{\phi}$, $\hat{z}$ after closing the α-integral in (1) for a magnetic current source along $\hat{y}$ are

$$\begin{aligned}
e_\rho(\vec{r}) &= -\frac{\cos\phi}{8\pi}\int_{-\infty}^{\infty}[V_{TM}(H_0-H_2)+V_{TE}(H_0+H_2)]\\
&\quad\times\tilde{M}_y e^{-jk_z z}k_\rho dk_\rho\\
e_\phi(\vec{r}) &= \frac{\sin\phi}{8\pi}\int_{-\infty}^{\infty}[V_{TM}(H_0+H_2)+V_{TE}(H_0-H_2)]\\
&\quad\times\tilde{M}_y e^{-jk_z z}k_\rho dk_\rho\\
e_z(\vec{r}) &= -\frac{j\zeta_d\cos\phi}{4\pi k_d}\int_{-\infty}^{\infty} I_{TM}H_1\tilde{M}_y e^{-jk_z z}k_\rho^2 dk_\rho\\
h_\rho(\vec{r}) &= -\frac{\sin\phi}{8\pi}\int_{-\infty}^{\infty}[I_{TE}(H_0-H_2)+I_{TM}(H_0+H_2)]\\
&\quad\times\tilde{M}_y e^{-jk_z z}k_\rho dk_\rho\\
h_\phi(\vec{r}) &= -\frac{\cos\phi}{8\pi}\int_{-\infty}^{\infty}[I_{TE}(H_0+H_2)+I_{TM}(H_0-H_2)]\\
&\quad\times\tilde{M}_y e^{-jk_z z}k_\rho dk_\rho\\
h_z(\vec{r}) &= -\frac{j\sin\phi}{4\pi\zeta_d k_d}\int_{-\infty}^{\infty} V_{TE}H_1\tilde{M}_y e^{-jk_z z}k_\rho^2 dk_\rho
\end{aligned}$$

in which the arguments $V_{TM/TE} = V_{TM/TE}(k_\rho)$, $I_{TM/TE} = I_{TM/TE}(k_\rho)$, $H_0 = H_0^{(2)}(k_\rho\rho)$, $H_1 = H_1^{(2)}(k_\rho\rho)$, $H_2 = H_2^{(2)}(k_\rho\rho)$ and $\tilde{M}_y = \tilde{M}_y(k_\rho,\phi)$ have been suppressed.

Appendix B

The leaky-wave modal electric and magnetic field components $\hat{\rho}$, $\hat{\phi}$, $\hat{z}$ due to a leaky-wave pole k_ρ^{LWP} are given by

$$\begin{aligned}
e_\rho^{LWP}(\vec{r}) &= -\frac{j\cos\phi}{4}k_\rho^{LWP}[Res(V_{TM})(H_0-H_2)\\
&\quad+Res(V_{TE})(H_0+H_2)]\tilde{M}_y\\
e_\phi^{LWP}(\vec{r}) &= \frac{j\sin\phi}{4}k_\rho^{LWP}[Res(V_{TM})(H_0+H_2)\\
&\quad+Res(V_{TE})(H_0-H_2)]\tilde{M}_y\\
e_z^{LWP}(\vec{r}) &= \frac{\zeta_d\cos\phi}{2k_d}\left(k_\rho^{LWP}\right)^2 Res(I_{TM})H_1\tilde{M}_y\\
h_\rho^{LWP}(\vec{r}) &= -\frac{j\sin\phi}{4}k_\rho^{LWP}[Res(I_{TM})(H_0+H_2)\\
&\quad+Res(I_{TE})(H_0-H_2)]\tilde{M}_y\\
h_\phi^{LWP}(\vec{r}) &= -\frac{j\cos\phi}{4}k_\rho^{LWP}[Res(I_{TM})(H_0-H_2)\\
&\quad+Res(I_{TE})(H_0+H_2)]\tilde{M}_y\\
h_z^{LWP}(\vec{r}) &= \frac{\sin\phi}{2\zeta_d k_d}\left(k_\rho^{LWP}\right)^2 Res(V_{TE})H_1\tilde{M}_y
\end{aligned}$$

where $Res(\cdot)$ indicates the evaluation of the residue at the pole and the arguments $V_{TM/TE} = V_{TM/TE}(k_\rho^{LWP})$, $I_{TM/TE} = I_{TM/TE}(k_\rho^{LWP})$, $H_0 = H_0^{(2)}(k_\rho^{LWP}\rho)$, $H_1 = H_1^{(2)}(k_\rho^{LWP}\rho)$, $H_2 = H_2^{(2)}(k_\rho^{LWP}\rho)$ and $\tilde{M}_y = \tilde{M}_y(k_\rho^{LWP},\phi)$ have been suppressed. Note that these expressions are only valid when $\theta > \theta_{SB}$ as described in Section III.

References

[1] D. R. Jackson and A. A. Oliner, "A leaky-wave analysis of the high-gain printed antenna configuration," *IEEE Trans. Antennas Propag.*, vol. AP-36, no. 7, pp. 905–910, Jul. 1988, doi: 10.1109/8.7194.

[2] G. Von Trentini, "Partially reflecting sheet arrays," *IRE Trans. Antennas Propag.*, vol. 4, no. 4, pp. 666–671, Oct. 1956, doi: 10.1109/TAP.1956.1144455.
[3] N. Guerin, S. Enoch, G. Tayeb, P. Sabouroux, P. Vincent, and H. Legay, "A metallic Fabry–Pérot directive antenna," *IEEE Trans. Antennas Propag.*, vol. 54, no. 1, pp. 220–224, Jan. 2006, doi: 10.1109/TAP.2005.861578.
[4] A. Hosseini, F. Capolino, and F. De Flaviis, "Gain enhancement of a V-band antenna using a Fabry–Pérot cavity with a self-sustained all-metal cap with FSS," *IEEE Trans. Antennas Propag.*, vol. 63, no. 3, pp. 909–921, Mar. 2015, doi: 10.1109/TAP.2014.2386358.
[5] H. Attia, M. L. Abdelghani, and T. A. Denidni, "Wideband and high-gain millimeter-wave antenna based on FSS Fabry–Pérot cavity," *IEEE Trans. Antennas Propag.*, vol. 65, no. 10, pp. 5589–5594, Oct. 2017, doi: 10.1109/TAP.2017.2742550.
[6] Q.-Y. Guo and H. Wong, "155 GHz dual-polarized Fabry–Pérot cavity antenna using LTCC-based feeding source and phase-shifting surface," *IEEE Trans. Antennas Propag.*, vol. 69, no. 4, pp. 2347–2352, Apr. 2021, doi: 10.1109/TAP.2020.3019528.
[7] N. Llombart, G. Chattopadhyay, A. Skalare, and I. Mehdi, "Novel terahertz antenna based on a silicon lens fed by a leaky wave enhanced waveguide," *IEEE Trans. Antennas Propag.*, vol. 59, no. 6, pp. 2160–2168, Jun. 2011, doi: 10.1109/TAP.2011.2143663.
[8] R. Gardelli, M. Albani, and F. Capolino, "Array thinning by using antennas in a Fabry–Pérot cavity for gain enhancement," *IEEE Trans. Antennas Propag.*, vol. 54, no. 7, pp. 1979–1990, Jul. 2006.
[9] A. Neto, N. Llombart, G. Gerini, M. D. Bonnedal, and P. de Maagt, "EBG enhanced feeds for the improvement of the aperture efficiency of reflector antennas," *IEEE Trans. Antennas Propag.*, vol. 55, no. 8, pp. 2185–2193, Aug. 2007, doi: 10.1109/TAP.2007.901854.
[10] S. A. Muhammad, R. Sauleau, and H. Legay, "Small-size shielded metallic stacked Fabry–Pérot cavity antennas with large bandwidth for space applications," *IEEE Trans. Antennas Propag.*, vol. 60, no. 2, pp. 792–802, Feb. 2012, doi: 10.1109/TAP.2011.2173133.
[11] M. A. Campo, D. Blanco, S. Bruni, A. Neto, and N. Llombart, "On the use of fly's eye lenses with leaky-wave feeds for wideband communications," *IEEE Trans. Antennas Propag.*, vol. 68, no. 4, pp. 2480–2493, Apr. 2020, doi: 10.1109/TAP.2019.2952474.
[12] A. Lalbakhsh, M. U. Afzal, K. P. Esselle, and S. L. Smith, "Wideband near-field correction of a Fabry–Pérot resonator antenna," *IEEE Trans. Antennas Propag.*, vol. 67, no. 3, pp. 1975–1980, Mar. 2019, doi: 10.1109/TAP.2019.2891230.
[13] L. Zhou, X. Duan, Z. Luo, Y. Zhou, and X. Chen, "High directivity Fabry–Pérot antenna with a nonuniform partially reflective surface and a phase correcting structure," *IEEE Trans. Antennas Propag.*, vol. 68, no. 11, pp. 7601–7606, Nov. 2020, doi: 10.1109/TAP.2020.2982514.
[14] A. Lalbakhsh, M. U. Afzal, K. P. Esselle, and S. L. Smith, "Low-cost nonuniform metallic Lattice for rectifying aperture near-field of electromagnetic bandgap resonator antennas," *IEEE Trans. Antennas Propag.*, vol. 68, no. 5, pp. 3328–3335, May 2020, doi: 10.1109/TAP.2020.2969888.
[15] T. N. Kaifas, D. G. Babas, G. Toso, and J. N. Sahalos, "Multibeam antennas for global satellite coverage: Theory and design," *IET Microw., Antennas Propag.*, vol. 10, no. 14, pp. 1475–1484, Nov. 2016, doi: 10.1049/iet-map.2015.0811.
[16] M. Alonso-delPino, S. Bosma, C. Jung-Kubiak, G. Chattopadhyay, and N. Llombart, "Wideband multimode leaky-wave feed for scanning lens-phased array at submillimeter wavelengths," *IEEE Trans. THz Sci. Technol.*, vol. 11, no. 2, pp. 205–217, Mar. 2021, doi: 10.1109/TTHZ.2020.3038033.
[17] H. Zhang, S. Bosma, A. Neto, and N. Llombart, "A dual-polarized 27 dBi scanning lens phased array antenna for 5G point-to-point communications," *IEEE Trans. Antennas Propag.*, vol. 69, no. 9, pp. 5640–5652, Sep. 2021.
[18] R. Maximidis, D. Caratelli, G. Toso, and A. B. Smolders, "High-gain planar array of reactively loaded antennas for limited scan range applications," *Electronics*, vol. 9, no. 9, p. 1376, Aug. 2020, doi: 10.3390/electronics9091376.
[19] D. Blanco, N. Llombart, and E. Rajo-Iglesias, "On the use of leaky wave phased arrays for the reduction of the grating lobe level," *IEEE Trans. Antennas Propag.*, vol. 62, no. 4, pp. 1789–1795, Apr. 2014, doi: 10.1109/TAP.2013.2272573.
[20] F. Scattone, M. Ettorre, B. Fuchs, R. Sauleau, and N. J. G. Fonseca, "Synthesis procedure for thinned leaky-wave-based arrays with reduced number of elements," *IEEE Trans. Antennas Propag.*, vol. 64, no. 2, pp. 582–590, Feb. 2016, doi: 10.1109/TAP.2015.2509008.
[21] D. Blanco, E. Rajo-Iglesias, A. M. Benito, and N. Llombart, "Leaky-wave thinned phased array in PCB technology for telecommunication applications," *IEEE Trans. Antennas Propag.*, vol. 64, no. 10, pp. 4288–4296, Oct. 2016, doi: 10.1109/TAP.2016.2597642.
[22] G. Lovat, P. Burghignoli, and D. R. Jackson, "Fundamental properties and optimization of broadside radiation from uniform leaky-wave antennas," *IEEE Trans. Antennas Propag.*, vol. 54, no. 5, pp. 1442–1452, May 2006, doi: 10.1109/TAP.2006.874350.
[23] M. Alonso-DelPino *et al.*, "Design guidelines for a terahertz silicon micro-lens antenna," *IEEE Antennas Wireless Propag. Lett.*, vol. 12, pp. 84–87, 2013.
[24] L. B. Felsen and N. Marcuvitz, *Radiation and Scattering of Waves*. Englewood Cliffs, NJ, USA: Prentice-Hall, 1973.
[25] S. Maci and A. Neto, "Green's function of an infinite slot printed between two homogeneous dielectrics—Part II: Uniform asymptotic solution," *IEEE Trans. Antennas Propag.*, vol. 52, no. 3, pp. 666–676, Mar. 2004, doi: 10.1109/TAP.2004.825500.
[26] A. Polemi and S. Maci, "On the polarization properties of a dielectric leaky wave antenna," *IEEE Antennas Wireless Propag. Lett.*, vol. 5, pp. 306–310, 2006, doi: 10.1109/LAWP.2006.878889.
[27] P. Burghignoli, G. Lovat, F. Capolino, D. R. Jackson, and D. R. Wilton, "Modal propagation and excitation on a wire-medium slab," *IEEE Trans. Microw. Theory Techn.*, vol. 56, no. 5, pp. 1112–1124, May 2008, doi: 10.1109/TMTT.2008.921657.
[28] G. Lovat, R. Araneo, and S. Celozzi, "Dipole excitation of periodic metallic structures," *IEEE Trans. Antennas Propag.*, vol. 59, no. 6, pp. 2178–2187, Jun. 2011, doi: 10.1109/TAP.2011.2143660.
[29] F. Liang *et al.*, "Dyadic Green's functions for dipole excitation of homogenized metasurfaces," *IEEE Trans. Antennas Propag.*, vol. 64, no. 1, pp. 167–178, Jan. 2016, doi: 10.1109/TAP.2015.2501430.
[30] P. Burghignoli, "A leaky-wave analysis of the phase center in Fabry–Pérot cavity antennas," *IEEE Trans. Antennas Propag.*, vol. 60, no. 5, pp. 2226–2233, May 2012, doi: 10.1109/TAP.2012.2189734.
[31] H. Zhang, S. O. Dabironezare, G. Carluccio, A. Neto, and N. Llombart, "A Fourier optics tool to derive the plane wave spectrum of quasi-optical systems [EM programmer's notebook]," *IEEE Antennas Propag. Mag.*, vol. 63, no. 1, pp. 103–116, Feb. 2021.
[32] K. A. Michalski and J. R. Mosig, "Multilayered media Green's functions in integral equation formulations," *IEEE Trans. Antennas Propag.*, vol. 45, no. 3, pp. 508–519, Mar. 1997, doi: 10.1109/8.558666.
[33] M. A. Hickey, M. Qiu, and G. V. Eleftheriades, "A reduced surface-wave twin arc-slot antenna for millimeter-wave applications," *IEEE Microw. Wireless Compon. Lett.*, vol. 11, no. 11, pp. 459–461, Nov. 2001, doi: 10.1109/7260.966041.
[34] N. Llombart, A. Neto, G. Gerini, M. Bonnedal, and P. D. Maagt, "Impact of mutual coupling in leaky wave enhanced imaging arrays," *IEEE Trans. Antennas Propag.*, vol. 56, no. 4, pp. 1201–1206, Apr. 2008, doi: 10.1109/TAP.2008.919223.
[35] M. A. Campo *et al.*, "H-band quartz-silicon leaky-wave lens with air-bridge interconnect to GaAs front-end," *IEEE Trans. THz Sci. Technol.*, vol. 11, no. 3, pp. 297–309, May 2021, doi: 10.1109/TTHZ.2021.3049640.
[36] *CST Studio Suite*. Accessed: 2021. [Online], Available: https://www.3ds.com/products-services/simulia/products/cst-studio-suite/
[37] A. Neto and N. Llombart, "Wideband localization of the dominant leaky wave poles in dielectric covered antennas," *IEEE Antennas Wireless Propag. Lett.*, vol. 5, no. 1, pp. 549–551, Dec. 2006, doi: 10.1109/LAWP.2006.889558.
[38] C. P. Scarborough, J. P. Turpin, D. F. DiFonzo, and J. Finney, "Lens antenna system," U.S. Patent 20180269576, Oct. 2, 2017.

Sjoerd Bosma (Graduate Student Member, IEEE) received the B.Sc. and M.Sc. (*cum laude*) degrees in electrical engineering from the Delft University of Technology, Delft, The Netherlands (TU Delft), in 2015 and 2017, respectively. He is currently pursuing the Ph.D. degree with the Terahertz Sensing Group, TU Delft.

From September 2018 to February 2019, he participated in the JPL Visiting Student Researcher Program, Jet Propulsion Laboratory, Pasadena, CA, USA. He is working on leaky-wave lens antenna arrays for submillimeter-wave spectrometers with TU Delft.

Andrea Neto (Fellow, IEEE) received the Laurea degree (*summa cum laude*) in electronic engineering from the University of Florence, Florence, Italy, in 1994, and the Ph.D. degree in electromagnetics from the University of Siena, Siena, Italy, in 2000.

Part of his Ph.D. degree was developed at the European Space Agency Research and Technology Center, Noordwijk, The Netherlands, where he worked for the Antenna Section for over two years. From 2000 to 2001, he was a Post-Doctoral Researcher with the California Institute of Technology, Pasadena, CA, USA, where he worked with the Sub-Millimeter Wave Advanced Technology Group. From 2002 to January 2010, he was a Senior Antenna Scientist with TNO Defence, Security and Safety, The Hague, The Netherlands. In February 2010, he became a Full Professor of applied electromagnetism with the Electrical Engineering, Mathematics and Computer Science (EEMCS) Department, Technical University of Delft, Delft, The Netherlands, where he formed and leads the THz Sensing Group. His research interests include the analysis and design of antennas with an emphasis on arrays, dielectric lens antennas, wideband antennas, EBG structures, and THz antennas.

Dr. Neto is currently a member of the Technical Board of the European School of Antennas and an Organizer of the course on antenna imaging techniques. He is also a member of the Steering Committee of the Network of Excellence NEWFOCUS, dedicated to focusing techniques in millimeter- and sub-millimeterm-wave regimes. He was a recipient of the European Research Council (ERC) Starting Grant to perform research on advanced antenna architectures for THz sensing systems in 2011, the H. A. Wheeler Award for the Best Applications Paper of 2008 in the IEEE TRANSACTIONS ON ANTENNAS AND PROPAGATION, the Best Innovative Paper Prize of the 30th ESA Antenna Workshop in 2008, and the Best Antenna Theory Paper Prize of the European Conference on Antennas and Propagation (EuCAP) in 2010. He has served as an Associate Editor for the IEEE TRANSACTIONS ON ANTENNAS AND PROPAGATION from 2008 to 2013 and IEEE ANTENNAS AND WIRELESS PROPAGATION LETTERS from 2005 to 2013.

Nuria Llombart (Fellow, IEEE) received the master's degree in electrical engineering and the Ph.D. degree from the Polytechnic University of Valencia, Valencia, Spain, in 2002 and 2006, respectively.

During her master's degree studies, she spent one year at the Friedrich-Alexander University of Erlangen-Nuremberg, Erlangen, Germany. She worked with the Fraunhofer Institute for Integrated Circuits, Erlangen. From 2002 to 2007, she was a Ph.D. Student and a Researcher with the Antenna Group, TNO Defence, Security and Safety Institute, The Hague, The Netherlands. From 2007 to 2010, she was a Post-Doctoral Fellow with the California Institute of Technology, Pasadena, CA, USA, working with the Sub-Millimeter Wave Advanced Technology Group, Jet Propulsion Laboratory, Pasadena. From 2010 to 2012, she was a "Ramón y Cajal" Fellow with the Optics Department, Complutense University of Madrid, Madrid, Spain. In September 2012, she joined the THz Sensing Group, Technical University of Delft, Delft, The Netherlands, where she became a Full Professor in February 2018. She has coauthored more than 150 journal and international conference contributions. Her research interests include the analysis and design of planar antennas, periodic structures, reflector antennas, lens antennas, and waveguide structures, with emphasis in the THz range.

Dr. Llombart was a recipient of the H. A. Wheeler Award for the Best Applications Paper of 2008 in the IEEE TRANSACTIONS ON ANTENNAS AND PROPAGATION, the 2014 THz Science and Technology Best Paper Award of the IEEE Microwave Theory and Techniques Society, several NASA awards, the 2014 IEEE Antenna and Propagation Society Lot Shafai Mid-Career Distinguished Achievement Award, and the European Research Council (ERC) Starting Grant in 2015. She also serves as a Board Member for the IRMMW-THz International Society.